

Internal Gravity Wave Breaking in White Dwarf Binaries

Yubo Su,¹ Daniel Lecoanet,² Dong Lai,¹

¹ *Cornell Center for Astrophysics and Planetary Science, Department of Astronomy, Cornell University, Ithaca, NY 14853, USA*

² *Princeton Center for Theoretical Science, Princeton University, Princeton, NJ 08544, USA*

Accepted XXX. Received YYY; in original form ZZZ

ABSTRACT

In sufficiently compact white dwarf binaries, dynamical tides raise a train of internal gravity waves that propagate towards the surface. We perform 2D numerical simulations of these waves undergoing nonlinear wave breaking in an incompressible, isothermal atmosphere. After an initial transient phase, we find that these waves induce a sharp transition between a non-rotating core and synchronously rotating envelope. We find evidence that the width of this transition layer is bound from below by the Kelvin-Helmholtz Instability. We provide analytical formulae for absorption and reflection of incident waves off the critical layer up to prefactors of order unity. These prefactors converge to constant values when artificial dissipation is decreased. We provide dimensionless criteria necessary to resolving momentum transfer within the critical layer. Finally, we speculate on the application of our model to tidal synchronization and heating in astrophysical systems.

Key words: white dwarfs – hydrodynamics – binaries:close – waves

1 INTRODUCTION

[Below copied from proposal, will rewrite]

Compact white dwarf (WD) binary systems, with orbital periods in the range of minutes to hours, are important for a range of astrophysical problems. They are the most important sources of gravitational waves (GWs) for the Laser Interferometric Space Antenna (LISA) (Nelemans 2009). They are also thought to produce interesting optical transients such as underluminous supernovae (Perets et al. 2010), Ca-rich fast transients (García-Berro et al. 2017), and tidal novae (Fuller & Lai 2012b). Most importantly, they have been proposed as the likely progenitors of type Ia supernovae (e.g. Iben Jr & Tutukov 1984; Webbink 1984) or more recently (Gilfanov & Bogdán 2010; Maoz et al. 2010). While presently only a few tens of compact WD binaries are known (Korol et al. 2017), *Gaia* (currently gathering data) is expected to expand the catalog to a few hundreds (Korol et al. 2017) (results based on *Gaia*’s second data release have already begun to appear (Shen et al. 2018; Kilic et al. 2018)), and the Large Synoptic Survey Telescope (LSST, first light scheduled for 2020) will likely detect a few thousand more (Korol et al. 2017). These observations will significantly advance the understanding of WD binaries and their evolution. My proposed theoretical and computational research is well-timed to take advantage of these new advances.

In spite of the broad importance of WD binaries, the evolution of these systems prior to their final mergers is not well understood. Much of this uncertainty comes from our imprecise understanding of tidal interactions, which play an important role during a compact WD binary’s inspiral (Fuller & Lai 2012a). Previous studies have shown that these interactions manifest as tidal excitation of internal gravity waves (IGW), waves in the WD fluid restored by the

buoyancy force due to density stratification (Fuller & Lai 2011). As these waves propagate outwards towards the WD surface, they grow in amplitude until they break, as do ocean waves on a shore, and transfer both energy and angular momentum from the binary orbit to the outer envelope of the WD (Fuller & Lai 2011, 2012a).

Previous works have found that the dissipation of IGW can generate significantly more energy than thermal radiation from the isolated WD surface and is thus a major contributor to the WD energy budget (Fuller & Lai 2012a, 2013). However, these works parameterized the wave breaking process in an ad hoc manner. The details of dissipation, namely the location and spatial extent of the wave breaking, affect the observable outcome: dissipation near the surface of the WD can be efficiently radiated away and simply brightens the WD, while dissipation deep in the WD envelope causes an energy buildup that results in energetic flares (Fuller & Lai 2012b). Works in other fields based on numerical simulations show that strongly nonlinear wave breaking behaves differently than predictions based in linear and weakly nonlinear theory (Winters & D’Asaro 1994; Barker & Ogilvie 2010). Such fully nonlinear numerical simulations have not been performed for WDs.

In Section 2, we will describe the system of equations we will use to analyze IGW breaking. In Section 3, we discuss relevant analytical results. In Section 5 we present the results of numerical simulations. Finally, in Section 6 we discuss the results of the preceeding section.

2 PROBLEM DESCRIPTION

We consider a two-dimensional incompressible, isothermal fluid, representative of degenerate matter in WDs. We furthermore ne-

glect temperature variations and assume a barotropic equation of state $P(\rho, T) = P(\rho)$ as a first approximation. As we are interested in dynamics far from the center of the WD, we approximate the gravitational field as uniform. We model the background density stratification as $\bar{\rho}(x, z) = \bar{\rho}_0 e^{-z/H}$ for some reference density $\bar{\rho}_0$ (we generally notate background quantities with overbars and perturbation quantities with primes).

The Euler equations for an incompressible, barotropic fluid in a uniform gravitational field are

$$\nabla \cdot \mathbf{u} = 0, \quad (1a)$$

$$\frac{D\rho}{Dt} = 0, \quad (1b)$$

$$\frac{D\mathbf{u}}{Dt} + \frac{\nabla P}{\rho} + g\mathbf{z} = 0. \quad (1c)$$

$\frac{D}{Dt} = \frac{\partial}{\partial t} + (\mathbf{u} \cdot \nabla)$ is the Lagrangian or material derivative, and \mathbf{u}, ρ, P denote the velocity field, density and pressure respectively. We denote $-g\mathbf{z}$ constant gravitational acceleration. Note that at hydrostatic equilibrium $\frac{\partial}{\partial t} = 0$ we have $\nabla P = -\bar{\rho}g\mathbf{z}$ and so $\bar{P} = \bar{\rho}gH$. A vertically-stratified shear flow $\bar{u}_x(z)\mathbf{x}$ is permitted at hydrostatic equilibrium, but we will assume no background flow, so $\mathbf{u} = \mathbf{u}'$. Physically, this assumption corresponds to a non-rotating star, or going to the corotating frame of a rigidly rotating star.

In practice, it is convenient to introduce coordinate $\Upsilon = \ln \frac{\rho}{\bar{\rho}}$ (e.g. see (Lecoanet et al. 2014)). This both identically enforces $\rho > 0$ and avoids numerical issues in the $\frac{\nabla P}{\rho}$ term if ρ is small. We also define reduced pressure $\varpi = \frac{P}{\bar{\rho}}$. Then, we may rewrite the second two equations of Equation 1 as

$$\frac{D\Upsilon}{Dt} + u'_z \frac{\partial \ln \bar{\rho}}{\partial z} = 0, \quad (2a)$$

$$\frac{D\mathbf{u}'}{Dt} + \nabla \varpi + \varpi \nabla \Upsilon + g\mathbf{z} = 0. \quad (2b)$$

Note that in the new coordinates, hydrostatic equilibrium corresponds to $\Upsilon = 0, \bar{\varpi} = gH$.

3 INTERNAL GRAVITY WAVES: THEORY

3.1 Analytical Properties: Linear

In the small perturbation limit, where flow velocities are small compared to the characteristic space and time scales $\frac{\partial}{\partial t} \gg \mathbf{u}' \cdot \nabla$, we may linearize Equation 2. The solution in this linear regime up to undetermined amplitude A is given by (Drazin 1977; Dosser & Sutherland 2011b):

$$u'_z(x, z, t) = A e^{z/2H} e^{i(k_x x + k_z z - \omega t)}, \quad (3)$$

where ω satisfies dispersion relation

$$\omega^2 = \frac{N^2 k_x^2}{k_x^2 + k_z^2 + \frac{1}{4H^2}}. \quad (4)$$

We take

$$N^2 \equiv g^2 \left(\frac{d\rho}{dP} - \frac{1}{c_s^2} \right) = \frac{g}{H}, \quad (5)$$

the Brunt-Väisälä frequency to be constant in the incompressible limit $c_s \rightarrow \infty$ where c_s is the sound speed. Other dynamical quantities are simply related to u'_z (see e.g. Dosser & Sutherland (2011b)).

In the weak stratification limit $|k_z H| \gg 1$, the solution exhibits the following characteristics:

- The amplitude of the wave grows with z as $e^{z/2H}$. Thus, the linear approximation is always violated for sufficiently large z .
- The phase and group velocities are respectively:

$$\mathbf{c}_{ph} = (k_x \mathbf{x} + k_z \mathbf{z}) \frac{\omega}{k_x^2 + k_z^2 + \frac{1}{4H^2}}, \quad (6)$$

$$\mathbf{c}_g = N \frac{\left(k_z^2 + \frac{1}{4H^2} \right) \mathbf{x} - (k_x k_z \mathbf{z})}{\left(k_x^2 + k_z^2 + \frac{1}{4H^2} \right)^{3/2}}. \quad (7)$$

We note $\mathbf{c}_{ph} \cdot \mathbf{c}_g = O\left(\frac{1}{(k_z H)^2}\right) \approx 0$, the usual result (e.g. Drazin (1977); Dosser & Sutherland (2011a)). Note that for an upwards propagating IGW $c_{g,z} > 0, k_z < 0, k_x > 0$.

- The time-averaged total x -momentum flux F carried in the z direction can be computed. Since the linear solution consists of terms separable as $f(x, z, t) = f(z) e^{i(k_x x - \omega t)}$, x averaging and time averaging are equivalent. We may then write

$$F \equiv \langle \rho u'_x u'_z \rangle_x \equiv \frac{1}{L_x} \int_0^{L_x} \rho u'_x u'_z dx, \quad (8)$$

$$\approx -\frac{A^2}{2} \bar{\rho}_0 \frac{k_z}{k_x}, \quad (9)$$

where $\langle \dots \rangle_x$ denotes x -averaging. Note that indeed for an upwards propagating IGW $k_z < 0, k_x > 0$, we have $F > 0$.

3.2 Wave Generation: Analytical Analysis

Since we are only concerned with the behavior of the wave at high z where wave breaking occurs, we generate waves in the most numerically convenient way. As long as physically representative IGW are generated and wave dynamics are only examined far from the forcing region, the exact excitation mechanism is not important for our conclusions.

To model continuous excitation of IGWs deep in the WD interior propagating towards the surface, we use a volumetric forcing term to excite IGW near the bottom of the simulation domain¹. Our forcing excites both IGWs propagating upwards, imitating a wave tidally excited deeper in the WD, and downwards, which are damped away by the damping layers described in subsection 4.2.

As not to interfere with the incompressibility constraint, we force the system on the density equation. We implement forcing with strength C localized around z_0 with width σ by replacing Equation 2a with

$$\frac{D\Upsilon}{Dt} + u'_z \frac{\partial \ln \bar{\rho}}{\partial z} = C e^{-\frac{(z-z_0)^2}{2\sigma^2}} \cos(k_x x - \omega t). \quad (10)$$

Using a narrow Gaussian profile excites a broad z power spectrum, but only the k_z satisfying dispersion relation Equation 4 for the given $k_x, \omega(k_x, k_z)$ will propagate.

In the linearized system, the effect of this forcing can be solved analytically up to good accuracy: we first approximate the driving term using $e^{-\frac{(z-z_0)^2}{2\sigma^2}} \approx \sqrt{2\pi\sigma^2} \delta(z - z_0)$, the $\sigma \rightarrow 0$ limit². This system is solved exactly by matching the two plane wave solutions,

¹ Interfacial forcing is numerically unstable when using a Chebyshev polynomial basis in the z direction and impossible when using a Fourier basis.

² In practice, σ must be large enough to be numerically resolved by the spectral code.

above and below z_0 . We may then approximately relax the solution to nonzero σ : an extra factor of $e^{-\frac{(k_z \sigma)^2}{2}}$ arises compared to the δ -function solution (evaluating the Fourier Transform of $e^{-\frac{(z-z_0)^2}{2\sigma^2}}$ at k_z), and we obtain

$$u'_z(x, z, t) = \frac{C g k_x^2}{\omega^2} \frac{1}{2 i k_z} \frac{e^{-\frac{(k_z \sigma)^2}{2}}}{\sqrt{2 \pi \sigma^2}} \times \begin{cases} e^{\frac{z-z_0}{2H}} e^{i(k_x x + k_z(z-z_0) - \omega t + \frac{1}{2k_z H})} & z > z_0 \\ e^{\frac{z-z_0}{2H}} e^{i(k_x x - k_z(z-z_0) - \omega t + \frac{1}{2k_z H})} & z < z_0 \end{cases} \quad (11)$$

The $z > z_0$ region models an upwards-propagating IGW wavetrain excited deep in the atmosphere.

3.3 Wave Breaking Location

In developing the results above, we have neglected advective terms $\frac{\partial}{\partial t} \gg \mathbf{u}' \cdot \nabla$. However, since $|\mathbf{u}'| \propto e^{z/2H}$, any nonzero amplitude IGW will eventually violate the linearity criterion. This regime is relevant in practice since the IGW may grow to nonlinear amplitudes before it reaches the surface of the WD (Fuller & Lai 2011, 2012a). We can coarsely estimate the height at which this happens by when the Lagrangian displacement of the perturbation $\xi' = \frac{\mathbf{u}'}{-i\omega}$ of a fluid parcel satisfies

$$|\xi'| |\mathbf{k}| \sim \xi_z k_z \gtrsim 1. \quad (12)$$

This is in agreement with the breaking location predicted by the wave-induced mean flow, given by (Andrews & McIntyre 1976; Dosser & Sutherland 2011b):

$$\langle u_x \rangle \equiv \bar{U} = \frac{1}{L_x} \int u_x dx = \frac{\langle u_x u_z \rangle_x}{c_{g,z}}, \quad (13)$$

This formula is analogous to Stokes' drift for surface waves and can be derived by considering the propagation of F (Equation 8) into a medium at rest. Solving for $\bar{U} = \omega/k_x$ the critical layer condition (Equation 14 and discussion in subsection 3.4), we obtain $\left| \frac{u'_x k_x}{\omega} \right| = |\xi_x k_x| = |\xi_z k_z| \sim 1$, equal to the nonlinearity criterion Equation 12. This condition predicts where the wave's self-acceleration alone produces a critical layer.

3.4 Formation and Dynamics of Critical Layer

[TODO rewrite more clearly, it's just copy pasted together right now]

The general understanding of nonlinear IGW breaking is that the waves' interactions with the mean flow of the fluid transfer horizontal momentum from the waves into the fluid; such a process has been conjectured to be responsible for tidal synchronization in stellar binaries (Zahn 1975; Goldreich & Nicholson 1989) as well as the quasi-biennial oscillation (Lindzen & Holton 1968). The details of this process have been laid out in a few key papers: IGWs are globally unstable to resonant three-wave interactions (Drazin 1977), causing energy transfer out of the IGW to daughter modes. These steeper daughter modes facilitate wave breaking, depositing horizontal momentum in the fluid's mean flow (Klostermeyer 1991).

In accordance with literature and the simulation setup, we will assume momentum redistribution is inefficient (see subsection 6.1 for analysis of this assumption). The mean flow will then grow in place until it reaches the horizontal phase velocity of the parent

IGW. Then, a critical layer forms at which the frequency of the incident IGW is Doppler-shifted to zero. The interaction of the parent IGW with the mean flow was first studied in the inviscid, linear regime in (Booker & Bretherton 1967), which found nearly complete absorption. This result was reproduced with nonzero viscosity (Hazel 1967), but weakly nonlinear theory (Brown & Stewartson 1982) and fully nonlinear simulations (Winters & D'Asaro 1994) suggest that nonlinear effects can induce reflection.

A purely horizontal shear flow $\bar{U}(z)\mathbf{x}$ can be seen in Equation 1 to have the effect of modifying time derivatives ∂_t to their frequency in the comoving frame of the fluid $\partial_t - \bar{U}(z)\partial_x$. If anywhere $\bar{U}(z) = \bar{U}_c$ where

$$\bar{U}_c \equiv \omega/k_x, \quad (14)$$

then the horizontal wavenumber of the linear wave in the fluid frame vanishes and critical behavior is observed. In a linear theory, both inviscid (Booker & Bretherton 1967) and viscous (Hazel 1967), the incident wave has amplitude reflection and transmission coefficients

$$\text{Ri} \equiv \frac{N^2}{\left(\frac{\partial \bar{U}}{\partial z} \right)^2} \bigg|_{z_c}, \quad (15)$$

$$\mathcal{R}_A = e^{-2\pi \sqrt{\text{Ri} - \frac{1}{4}}}, \quad \mathcal{T}_A = e^{-\pi \sqrt{\text{Ri} - \frac{1}{4}}}, \quad (16)$$

where we have defined local Richardson number Ri at the critical layer z_c : $\bar{U}(z_c) = \frac{\omega}{k_x}$. In the $\text{Ri} \gg 1$ limit, $\mathcal{R}, \mathcal{T} \ll 1$ and the incident wave is completely absorbed to good approximation.

When the fluid absorbs the incident wave, it absorbs the incident horizontal momentum flux as well, which is converted into additional horizontal momentum of the shear flow. Since the mean flow cannot exceed \bar{U}_c the horizontal phase velocity of the incident wave, the critical layer must instead propagate downwards to accommodate the incident momentum. The total horizontal momentum of the shear flow then obeys conservation equation

$$\frac{\partial}{\partial t} \int \rho(z) \bar{U}(z, t) dz + \Delta F = 0. \quad (17)$$

ΔF is the total injected horizontal momentum to the flow. We next make a simple two-zone approximation $\bar{U}(z > z_c) = \bar{U}_c$, $\bar{U}(z < z_c) = 0$, assuming all horizontal momentum flux goes into critical layer propagation. Then, the conservation equation becomes simple differential equation

$$\rho(z_c) \bar{U}_c \frac{\partial z_c}{\partial t} = \Delta F. \quad (18)$$

If the entirety of the horizontal momentum flux carried by the IGW wavetrain is absorbed by the critical layer, then $\Delta F = -F'$ is constant in time. For constant ΔF in time and $\rho \approx \bar{\rho}$, $z_c(t)$ has analytical solution

$$z_c(t) = -H \ln t - H \ln \frac{H \bar{\rho}_0 \bar{U}_c}{-\Delta F}. \quad (19)$$

4 INTERNAL GRAVITY WAVES: LINEAR NUMERICAL SIMULATION

Towards numerical simulation of IGW breaking, we first verify agreement with linear theory at weak forcing amplitudes. We perform direct numerical simulation using the pseudo-spectral code Dedalus (Burns et al. 2016). In subsection 4.1 we discuss choices of numerical parameters, in subsection 4.2 we separately discuss use of a damping zone at the top and bottom of the domain, and

in [subsection 4.3](#) we present the results of our “linear” simulations, where we solve the full nonlinear fluid equations for weak forcing.

4.1 Numerical Setup

We nondimensionalize by taking $H = N = \bar{\rho}_0 = 1$.

Denote L_x, L_z to be the physical dimensions of the simulation domain. Our simulation domain is smaller than our full physical domain, so we adopt reflection-suppressing boundary conditions. We use periodic boundary conditions in the x direction and damping layers (described in [subsection 4.2](#)) in the z direction to damp perturbations exiting the top and bottom of the domain. We use a Fourier basis in both the x and z direction. We varied the number of x, z modes (denoted N_x, N_z respectively), and used 3/2 dealiasing ([Boyd 2001](#)).

The geometry of our simulation domain is fixed by three parameters: L_x, L_z , and z_0 the forcing location. We use $z_0 = 0.2L_z$ to force sufficiently far from the lower damping zone and permit sufficient room for the upwards-moving wave to grow at $\propto e^{z/2H}$. We choose $L_z = 10H$ to give $\sim e^3$ amplitude growth between the damping zones. Finally, we want similar grid spacing $\frac{L_x}{N_x} \sim \frac{L_z}{N_z}$. For computational savings, we fix $N_z = 4N_x$. We use $L_x = 4H = \frac{2}{5}L_z$.

The time integration uses a split implicit-explicit third-order scheme where certain terms are treated implicitly and the remaining terms are treated explicitly. A third-order, four-stage DIRK-ERK scheme ([Ascher et al. 1997](#)) is used with adaptive timesteps computed from advective Courant-Friedrichs-Lewy (CFL) time. Specifically, we use $\Delta t = 0.7 \min(\Delta x/u_x, \Delta z/u_z)$, where the minimum is taken over every grid point in the domain and $\Delta x, \Delta z$ are the grid spacings in the x and z directions respectively.

The physics of our simulation is fixed by four parameters: k_x, ω, C, ν . We describe our choices for these parameters below:

- k_x : Astrophysical IGWs in stars are generally excited by the $l = 2$ component of the tidal potential, for which $k_\perp \sim \frac{1}{R}$ where R is the radius of the star. To best emulate this, we use $k_x = \frac{2\pi}{L_x}$ the smallest permitted wavenumber permitted by periodic boundary conditions.

- ω : We choose ω by evaluating dispersion relation $\omega(k_x, k_z)$ for some desired k_z .

To choose k_z , we note astrophysical IGWs generally satisfy $\omega \ll N$, or equivalently $\frac{k_r}{k_\perp} \sim k_r R \gg 1$. Since $H \lesssim R$, we aim to study $k_z H \gg 1$. However, to satisfy this well is computationally expensive: $L_z \gg H$ is required to give waves ample room to grow within the simulation domain, but we want k_z to be sufficiently separated from the grid spacing $\sim L_z/N_z$ that nonlinear effects can be seen in later simulations (see [subsection 5.1](#)). Thus, N_z sets how well we can satisfy $k_z H \gg 1$; we choose $k_z H = 1$.

- C : We first choose C forcing strength such that $\xi_z k_z \ll 1$ is satisfied everywhere throughout the domain. This constrains C by [Equation 11](#).

- ν : Nonlinear effects transfer wave energy from \mathbf{k} to larger wavenumbers. Since well-resolved simulations using spectral methods have no inherent numerical viscosity, energy will accumulate at grid scales in the absence of artificial dissipation. We introduce dissipation parameter ν used for both artificial viscosity and artificial diffusivity. We ensure our equations of motion continue to conserve horizontal momentum (see [Appendix A](#) for details). Under weak forcing, we may set $\nu = 0$, since energy transfer out of the parent \mathbf{k} mode is negligible.

Finally, we use initial conditions $\mathbf{u}(x, z, 0) = \Upsilon(x, z, 0) =$

$0, \varpi(x, z, 0) = 1$ corresponding to hydrostatic equilibrium and no initial fluid motion.

4.2 Damping Layers

To imitate an infinite fluid using a finite simulation domain, we use periodic boundary conditions in the x direction and damping layers at the top and bottom of the z direction. This damps waves that reach the edge of the simulation domain without inducing nonphysical reflection. Specifically, we replace material derivatives in [Equation 2](#) with:

$$\frac{D}{Dt} \rightarrow \frac{D}{Dt} + \Gamma(z)\Upsilon, \quad \Gamma(z) = \frac{1}{2\tau} \left[2 + \tanh \frac{z - z_T}{\Delta z} + \tanh \frac{z_B - z}{\Delta z} \right], \quad (20)$$

where $z_B = 0.05L_z, z_T = 0.95L_z$ are the boundaries of the damping zone. This strongly damps perturbations below z_B and above z_T with damping time τ , negligibly affects dynamics between z_B, z_T and has transition width governed by Δz ; we use $\Delta z = 0.025L_z$. This prescription, used in similar studies ([Lecoanet et al. 2016](#)), has the advantage of being smooth, important for spectral methods. Further details of our implementation of the fluid equations in Dedalus are described in [Appendix A](#).

4.3 Simulation Results

We describe the results of a simulation satisfying the parameter choices in [subsection 4.1](#) such that $\xi_z k_z \ll 1$ everywhere.

During the simulation, we expect IGW of form [Equation 11](#) to be excited. The incompressibility constraint further yields a complete analytical solution for flow velocities $\mathbf{u}'_{al}(x, z, t)$. The amplitude of the observed IGW in the simulation field \mathbf{u} relative to analytical solution \mathbf{u}'_{al} over some region $z \in [z_b, z_t]$ can be estimated with estimator $\hat{A}_i(t)$ (subscript i denotes incident wave)

$$\hat{A}_i(t) = \frac{\int_{z_b}^{z_t} \int_0^{L_x} \bar{\rho} (\mathbf{u} \cdot \mathbf{u}'_{al}) dx dz}{\int_{z_b}^{z_t} \int_0^{L_x} \bar{\rho} (u'_{al})^2 dx dz} \quad (21)$$

If $\mathbf{u} = \mathbf{u}'_{al}$, then $\hat{A}_i(t) = 1$. The energy norm is a traditional normalization choice such that the overlap between $\mathbf{u}, \mathbf{u}'_{al} \propto e^{z/2H}$ is evenly weighted throughout the integration region.

For a simulation satisfying $\xi_z k_z \ll 1$ everywhere, we expect $\hat{A}_i(t) = 1$ when integrated between the forcing and damping zones, corresponding to choices $z_b \gtrsim z_0, z_t \lesssim z_T$ (z_0, z_T are defined in [Equation 10](#) and [Equation 20](#) respectively). For consistency with the nonlinear case later, we choose $z_b = z_0 + 3\sigma, z_t = z_b + H$ (using $z_t = z_T - \Delta z$ just below the damping layer instead does not change the results). The resulting measurement of $\hat{A}_i(t)$ is shown in [Figure 1](#).

The analytical theory also predicts that the horizontal momentum flux $F(z, t)$ should be spatially flat between the forcing zone where it is generated and the damping zone where it is dissipated ([Equation 8](#)). We make a slightly more accurate estimate of F the flux carried in the IGW by directly substituting \mathbf{u}'_{al} into [Equation 8](#). Calling this estimate

$$F'_{al} \equiv \frac{1}{L_x} \int_0^{L_x} \bar{\rho} u'_{al,x} u'_{al,z} dx, \quad (22)$$

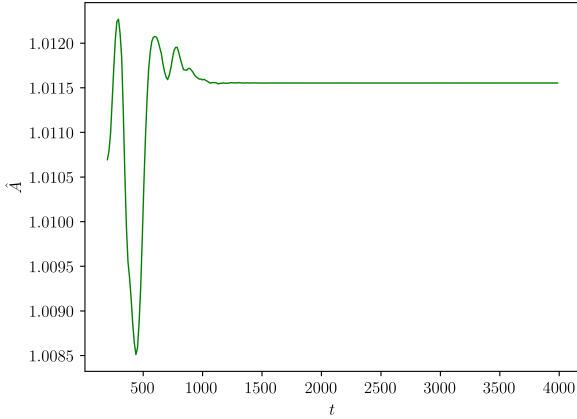


Figure 1. Amplitude of excited wave over time in weak forcing simulation, computed using Equation 21. $\hat{A}_i(t) = 1$ corresponds to perfect agreement with the analytical estimate. After an initial transient phase, we observe great agreement with Equation 11, and in particular $\hat{A}_i(t)$ asymptotes to a constant value, implying continuous excitation of identical IGW.

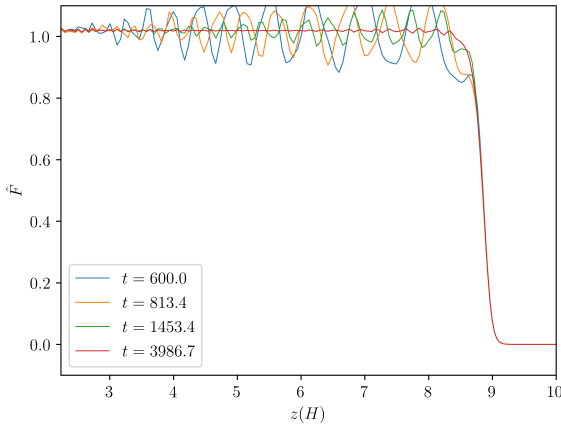


Figure 2. Equation 23 as a function of z at select times t . As initial transients die out, $\hat{F}(z, t) = 1$ to very good agreement above the forcing zone $z > z_0 = 2H$ and below the damping zone $z \lesssim z_T = 9.5H$. The flux excited in the forcing zone is transported without loss to the top of the domain, where it is dissipated by the damping layer (see subsection 4.2) without reflection.

we may then measure the agreement of our simulation with analytical expectation by computing

$$\hat{F}(z, t) \equiv \frac{\frac{1}{L_x} \int_0^{L_x} \rho u_x u_z \, dx}{F'_{al}}. \quad (23)$$

For our weak forcing simulation, $\hat{F} = 1$ is expected between z_0, z_T , and indeed we observe agreement with this in Figure 2.

Resolution	Re
1024 × 4096	2048
768 × 3072	1024
512 × 2048	512
256 × 1024	341
256 × 1024	205
256 × 1024	146

Table 1. Table of simulation resolutions. Note that Re is defined as in Equation 24.

5 INTERNAL GRAVITY WAVES: NONLINEAR SIMULATION

To perform simulations of wave breaking phenomena, we use the same values as subsection 4.1 except for C, ν . In particular, we choose C such that $\xi_z k_z|_{z_0} = 0.1$ in the forcing zone, which implies $\xi_z k_z$ exceeds 1 before z_T the upper damping zone. The dissipation parameter ν was varied across the various simulations. To quantify ν , we define dimensionless Reynolds number

$$\text{Re} \equiv \frac{\omega}{\nu k_z^2}. \quad (24)$$

A table of our simulation viscosities can be found in Table 1.

5.1 Numerical Simulation Results

A full video of our higher-resolution run at $N_x = 768, N_z = 3072, \text{Re} = 1024$ is available online³. We take this to be our fiducial simulation for the remainder of this paper, though other simulations show qualitatively identical behavior. Snapshots of the velocity field \mathbf{u} at select times can be found in Figure 3.

Slices of \bar{U}, \hat{F} across z at various times t are shown in Figure 4. While the behavior of \bar{U} seems to conform qualitatively with the predictions of subsection 3.4, the behavior of \hat{F} exhibits two salient features: (i) the incident flux seems to fluctuate greatly with time, and (ii) there seems to be a small transmitted feature at many of the later times. We will discuss further these features in subsection 5.4, after first analyzing the propagation of the critical layer.

5.2 Propagating Critical Layer

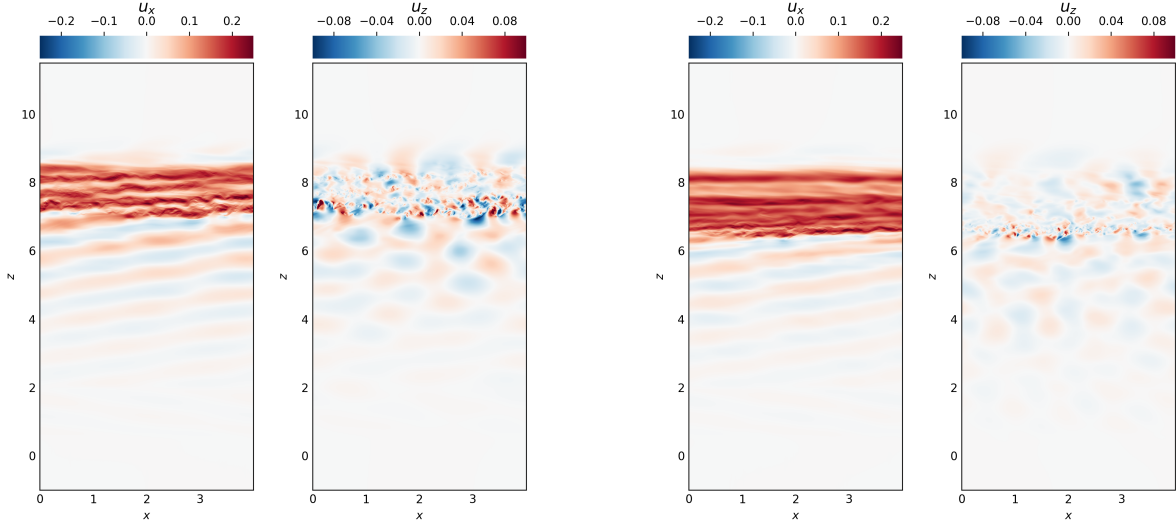
For the simulation shown in Figure 4, we may analyze the location of the critical layer. As the simulations are very noisy, we measure the location of the critical layer using an average of where flux deposition occurs

$$\begin{aligned} z_{c,\min} &= \underset{z}{\operatorname{argmin}} \{z : F(z) < 0.3F'_{al}\}, \\ z_{c,\max} &= \underset{z}{\operatorname{argmax}} \{z : F(z) > 0.3F'_{al}\}, \\ z_c &\equiv \frac{z_{c,\min} + z_{c,\max}}{2}. \end{aligned} \quad (25)$$

This was found to be a relatively stable estimator of the critical layer location. Other estimators were used and do not significantly change the results of the analysis.

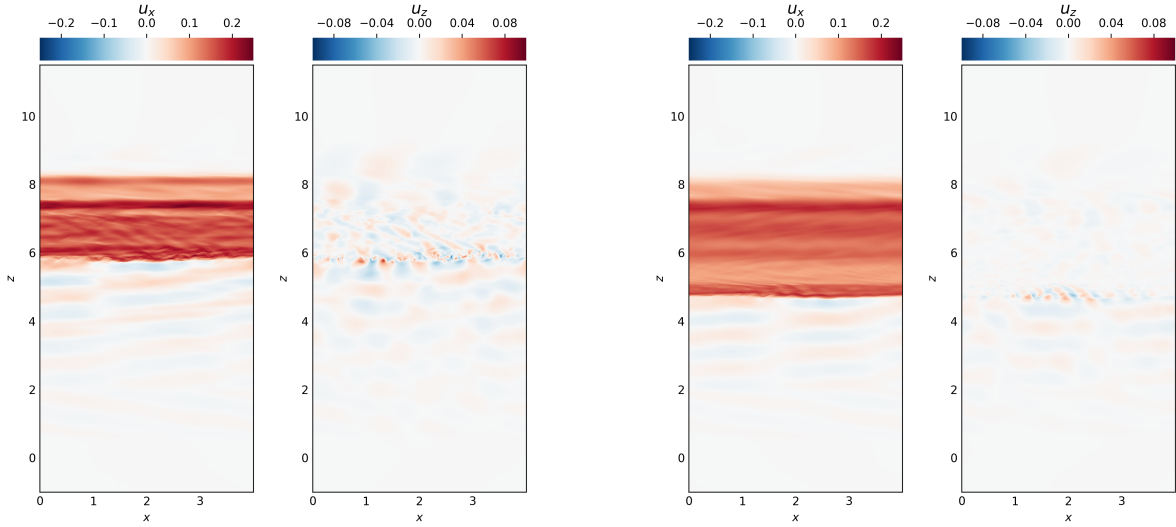
The evolution of z_c depends on the deposited flux $\Delta F(t)$ per Equation 18. To estimate $\Delta F(t)$ across the critical layer z_c from the

³ http://www.princeton.edu/~lecoanet/data/breaking_wave.mov



(a) $t = 413.4$ At early times, the flow resembles a linear IGW lower in the simulation domain but breaks down into smaller-scale features at higher z . Some characteristic swirling motion can be seen in both u_x , u_z , highly suggestive of Kelvin-Helmholtz instabilities.

(b) $t = 658.5$ At a slightly later time, the mean flow in u_x has become much more prominent and the critical layer z_c has become much more definite. Small-scale fluctuations are still present in u_z albeit at smaller amplitudes due to being in a denser region of the fluid.



(c) $t = 1171.4$ The critical layer transition is now extremely sharp, and small swirls of limited vertical extent at the location of the critical layer in u_z suggest that the Kelvin-Helmholtz instability is responsible for regulating the minimum width of this transition, a hypothesis explored in subsection 5.3.

(d) $t = 3437.8$ The end of the simulation shows very few significant qualitative differences from the previous snapshot, suggesting that the latter half of our simulation is temporally converged.

Figure 3. Snapshots of u_x , u_z in the fiducial simulation illustrating distinct phases of the evolution of the flow. Note that $\overline{U}_c \approx 0.16$ for the parameters used.

data, we defined:

$$F_<(t) = \langle F(z) \rangle_{z \in [z_c - \Delta z - H, z_c - \Delta z]}, \quad (26)$$

$$F_>(t) = \langle \{F(z) : F(z) < 0\} \rangle_{z \in [z_c, z_c + \Delta z]}, \quad (27)$$

$$\Delta F(t) \equiv F_>(t) - F_<(t). \quad (28)$$

$\langle \dots \rangle_{z \in [z_a, z_b]}$ denotes averaging over interval $[z_a, z_b]$. Below the critical layer, we average over an interval of length $H = \frac{2\pi}{k_z}$ a full vertical wavelength. The offset Δz is necessary to make a measurement of the incident flux unaffected by the turbulence within the

critical layer. The height of the critical layer is limited by $\text{Ri} \lesssim 1$, which bounds its vertical extent $\sim \frac{1}{k_z}$. Here, we found $\Delta z = \frac{3}{k_z}$ was necessary to be sufficiently offset from strong fluctuations near the critical layer.

Above the critical layer, waves decay over a much smaller vertical extent as they have larger z wavenumbers thanks to the shear flow, so we average over a Δz . Accurate measurement of these fluctuations above the critical layer is important to measuring the transmission feature accurately, seen in Figure 4 to be weak and attenuate quickly.

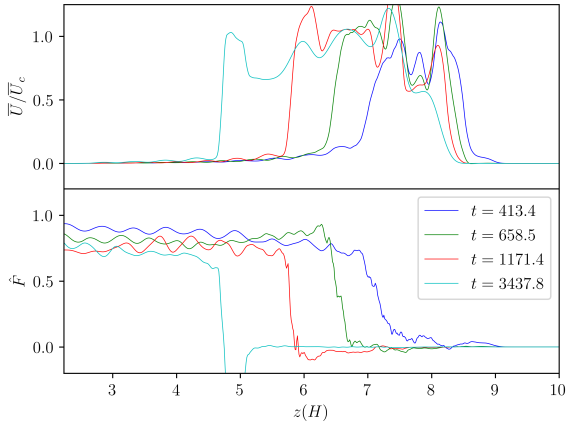


Figure 4. Plot of $\bar{U}(z, t)$ and $\hat{F}(z, t)$ respectively at various times over z in our $\text{Re} = 1024$ simulation. \bar{U} , \hat{F} follow their definitions in Equation 13 and Equation 23. \bar{U} is given in units of $\bar{U}_c = \frac{\omega}{k_x}$ the critical horizontal flow velocity (see subsection 3.4). The propagation of the critical layer towards lower z and sharp deposition of F at the critical layer are evident.

Finally, we may plot the observed z_c from data against two simple predictors: (i) integration of Equation 18 using the measured $\Delta F(t)$, and (ii) substituting the time-averaged $\langle \Delta F \rangle_t$ into Equation 19. Since $z_c(t)$ is both stable and less well-defined at early times (when the critical layer is thick and transient behavior is still strong), we instead integrate backwards from the end of the simulation, using $z_c(t_f)$ as initial condition. The resulting predictors are depicted in Figure 5. The good agreement between the evolution of $z_c(t)$ and its estimate via $\Delta F(t)$ and Equation 18 are noteworthy. Further of interest is the discrepancy between the time-averaged predictor and the data. The general agreement clearly demonstrates $\Delta F < F'_{al}$ and that incomplete absorption is observed. Moreover, its significant underprediction of critical layer motion at early times contrasts with its comparatively satisfactory prediction at later times to indicate that $\Delta F(t)$ must vary significantly over time. Both of these observations indicate a careful characterization of reflectivity is necessary.

5.3 Kelvin-Helmholtz Instability and Critical Layer Width

The observation of reflected/transmitted waves is in accordance with previous studies as discussed in subsection 3.3. Studies have shown that a local Richardson number $\text{Ri} \sim 1/4$ corresponds to the onset of reflectivity. This Ri also corresponds to the onset of the Kelvin-Helmholtz instability (KHI). Indeed, in our simulations, visual inspection suggests the KHI is present in the critical layer (see Figure 3). It is natural to suspect then that the shear flow cannot steepen any further than KHI onset. To verify this, we decided to compute a local Ri for the shear flow around the critical layer.

Since fluid instabilities are local, Ri must be measured in the immediate vicinity of a fluid parcel. Thus, we first assign an Ri for every x in the critical layer, then take the median as Ri for the entire layer. To avoid noisiness, the local Ri is computed using the vertical distance over which the local u_x increases from $0.3 \times$ its critical value to its critical value. The value 0.3 effectively excludes

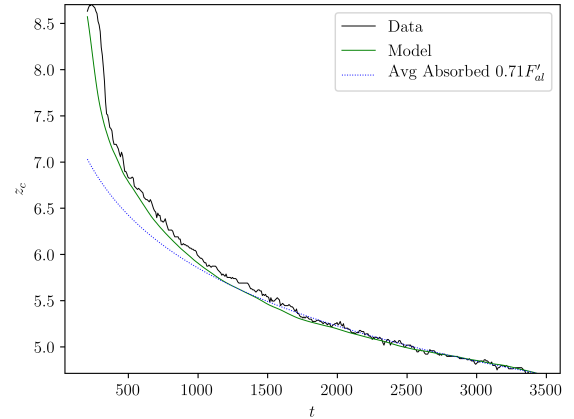


Figure 5. Propagation of the critical layer over time. Shown are (black) $z_c(t)$ from simulation data, (green) predictor of $z_c(t)$ using direct integration of Equation 18 for $\Delta F(t)$ measured from simulation data (described in Equation 28) and (blue) direct substitution of time-averaged $\langle \Delta F(t) \rangle_t$ into Equation 19. Predictors use the end of the simulation as initial conditions and integrate backwards, as z_c is less well-defined at early times. The agreement of the directly-integrated predictor with the data shows Equation 18 is a good description of the evolution of z_c . The poorer but qualitatively correct agreement of the time-averaged predictor with the data shows both that $\Delta F(t) \neq F'_{al}$ and that $\Delta F(t)$ likely has some very real variation with time.

the self-acceleration induced by the IGW. This can be written

$$\begin{aligned} z_{CL, \min}(x, t) &= \underset{\zeta}{\operatorname{argmin}} \left\{ z : u_x(x, \zeta, t) > 0.3 \bar{U}_c \right\}, \\ z_{CL, \max}(x, t) &= \underset{\zeta}{\operatorname{argmax}} \left\{ z : u_x(x, \zeta, t) < \bar{U}_c \right\}, \\ \text{Ri}(t) &\equiv \underset{x}{\operatorname{med}} \left(\frac{N^2(z_{CL, \max} - z_{CL, \min})^2}{(0.7 \bar{U}_c)^2} \right). \end{aligned} \quad (29)$$

To understand the variation in Ri over x , we can also plot using the minimum over x (the maximum is significantly noisier). Both of these are shown in Figure 6. The quick evolution of Ri to its saturated value is reflective of the fact that IGW are *anti-diffusive*. This property is a simple consequence of the IGW dispersion relation Equation 4, which is approximately $\omega k_z \approx N k_x$ such that as an IGW propagates into a shear flow, ω decreases and k_z increases, enhancing dissipation and further driving mean flow acceleration.

5.4 Non-absorption at Critical Layer

We identify two instances of non-absorptive behavior: (i), the presence of a reflected wave with wave vector $\mathbf{k} = k_x \mathbf{x} + k_z \mathbf{z}$, and (ii) the amount of horizontal momentum flux F reflected off the critical layer.

To measure the reflected wave amplitude, we use almost the same definition Equation 21 except using $k_z \rightarrow -k_z$; call this estimated $\hat{A}_r(t)$ the amplitude of the downwards-propagating reflected wave. To compute $\hat{A}_r(t)$, we furthermore permit an arbitrary phase offset $\phi_r(t)$ at each time t , since the phase of the reflected wave is unknown, unlike that of the incident wave. $\phi_r(t)$ in our simulations behaves in agreement with reflection off a moving boundary at z_c , well approximated by $\left| \frac{\partial \phi_r}{\partial t} \right| \approx 2 \left| \frac{\partial(k_z z_c)}{\partial t} \right|$.

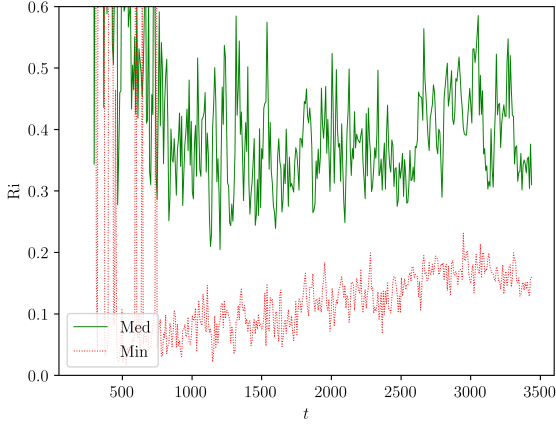


Figure 6. Local Richardson number of the flow at the critical layer over time as defined in Equation 29. Dotted red lines demarcate the minimum and median of Ri over x . These numbers effectively measure the mean and spread in width of the critical layer over x . Note that $Ri \sim \frac{1}{4}$ corresponds to the KHI, so this plot suggests the shear at the critical layer does not steepen past the KHI onset.

Since reflectivity depends sensitively on accurate measurements of \hat{A}_i , \hat{A}_r , we remark Equation 21 ensures orthogonality between $k_x \mathbf{x} \pm k_z \mathbf{z}$ modes. The integral for \hat{A}_r is also performed over $z \in [z_0 + 3\sigma, z_0 + 3\sigma + H]$. Since $\hat{A}_i(t)$, $\hat{A}_r(t)$ vary somewhat over time, we perform time averaging over interval approximately $8\pi/\omega$, denoted by angle brackets. We can then define the amplitude reflectivity

$$\mathcal{R}_A(t) \equiv \frac{\langle \hat{A}_r \rangle(t)}{\langle \hat{A}_i \rangle(t)}. \quad (30)$$

To measure the reflected horizontal momentum flux, we recall from our linear simulations described in subsection 4.3 that we are able to accurately predict the incident flux from the incident wave amplitude. Thus, we write for incident flux

$$F_i(t) \equiv \langle \rho u_x u_z \rangle_x \hat{A}_i^2(t). \quad (31)$$

But then, since we already have $\Delta F(t)$, $F_>(t)$ jump and transmitted flux across the critical layer at time t respectively, we can immediately write down the reflected flux

$$F_d(t) = F_i(t) + \Delta F(t) - F_>(t). \quad (32)$$

Then we can define flux reflectivity and transmissivity coefficients

$$\mathcal{R}_F(t) \equiv -\frac{\langle F_d \rangle(t)}{\langle F_i \rangle(t)}, \quad \mathcal{T}_F(t) \equiv -\frac{\langle F_> \rangle(t)}{\langle F_i \rangle(t)}. \quad (33)$$

The measurements of \hat{A}_i , \hat{A}_r , F_i , ΔF , F_d , $F_>$ are given in Figure 7. The oscillations in \hat{A}_i , F_i , A_d , F_d are apparent but the mean values seem to have temporally converged.

Using these measured quantities, we may make plots of \mathcal{R}_A^2 , \mathcal{R}_F , \mathcal{T}_F , which are provided in Figure 8. A comparison between \mathcal{R}_A^2 and \mathcal{R}_F is appropriate as $F \propto A^2$. Visual inspection suggests the three quantities have reached their asymptotic values after $t \gtrsim 1750/N$. An observation may be made that in general $\mathcal{R}_F \geq \mathcal{R}_A^2$; this conforms to the expectation that reflected flux consists of the simple reflected mode and higher order modes as well.

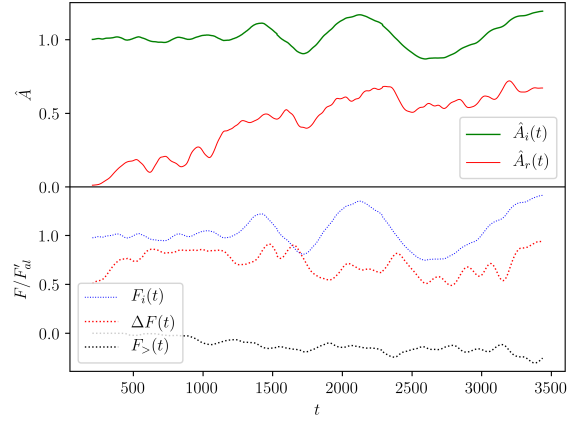


Figure 7. The top panel measures the incident wave amplitude $\hat{A}_i(t)$ (green) and the downwards propagating wave amplitude $\hat{A}_r(t)$ (red) just above the forcing zone, normalized to the analytical estimate Equation 11. $A_d \neq 0$ due to reflection off the critical layer. The bottom panel shows the behavior of three horizontal momentum fluxes over time, in units of the analytical estimate Equation 9: (blue) flux incident on the critical layer, (red) flux absorbed by the critical layer, and (black) flux transmitted through the critical layer.

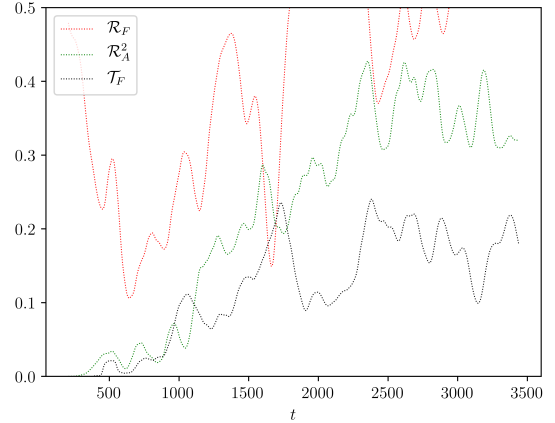


Figure 8. Reflectivity and transmissivity coefficients for flux and amplitude-squared as described by Equation 30 and Equation 33 respectively. The coefficients seem to become comparatively stable past about $t = 1750/N$, indicating that an asymptotic value may have been reached.

5.5 Convergence

As the primary test of convergence in our previous sections, we consider the convergence of the physically significant parameters of our model. In particular, the convergence of Ri, shown in Figure 6, and of the reflection/transmission coefficient asymptotic values, shown in Figure 8, are of greatest significance.

To estimate convergence, we compute the median value of each of Ri, \mathcal{R}_A^2 , \mathcal{R}_F , \mathcal{T}_F over the last 1/4 of simulation times from each simulation, where all simulations had converged to what appeared to be asymptotic values. Error bars are estimated with the 16 and 84

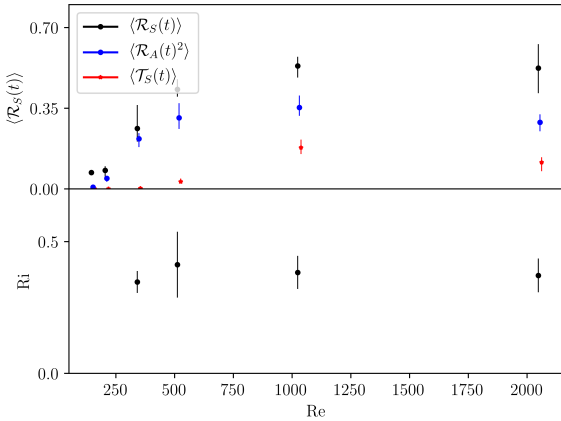


Figure 9. Convergence of median reflection/transmission coefficients and Ri (critical layer width) across runs with varying viscosity, parameterized with Re (Equation 24). Error bars depict 16 and 84 percentile values. Small horizontal displacements are made for data points at identical Re for readability. Note that simulations with larger Re correspond to smaller viscosity and are more physically realistic, and our values seem to converge towards large Re . At the smallest Re value, $Ri \approx 50$ is too large to fit on the plot.

percentiles. We illustrate the convergence of these averages across simulations in Figure 9.

It is apparent that the Richardson number rapidly converges to $Ri \approx 0.4$ but the reflection/transmission coefficients converge more slowly. This is in disagreement with Equation 16 calculated via the linear analytical theory. This tension is natural: fluid motion within the critical layer is turbulent, so transmission/reflection at the critical layer cannot be captured by any linear theory.

6 DISCUSSION

In the previous section, we have argued for a continuous train of breaking IGWs spontaneously forming a critical layer and strong shear flow. We have parameterized the width of the critical layer as well as horizontal momentum transport near the critical layer. In the subsequent sections, we will discuss the validity of these results and their application to astrophysical systems.

6.1 Physical Sources of Dissipation in WDs

The most significant linear damping in WD g-modes comes from radiative damping (Fuller & Lai 2011). In (Wu 1998) and (Fuller & Lai 2011), the radiative damping rate is given in terms of $\omega_i = \gamma \omega_r$, where ω_r is the frequency of the g-mode. Typical values for γ range from 10^{-4} to 10^{-11} depending on n of the g-mode.

We will assume this prescription directly transfers to propagating IGW, which results in general agreement with (Burkart et al. 2013)’s estimate of radiative damping rates. Then, making coarse identification $\omega_i \sim \nu k^2 \approx \nu k_z^2$, we find that $Re \sim \frac{1}{\gamma}$. Even at $\gamma = 10^{-4}$ however, the corresponding Re is far too weak to suppress reflection/transmission at the critical layer (e.g. Figure 9).

Another source of dissipation considered in (Burkart et al. 2013) is turbulent convective damping. They find this damping rate to never exceed that of radiative damping, and so it is also too weak to suppress critical layer formation in our problem.

Finally, we consider the impact of magnetic winding. In (Burkart et al. 2013), magnetic winding is used to enforce solid body rotation on the grounds that $t_A \gg t_{gw}$, where

$$t_A = \int_0^R \frac{\sqrt{4\pi\rho}}{B_0} dr \sim 10^2 \text{ yr} (*) \frac{10^3 \text{ G}}{B}. \quad (34)$$

the Alfvén wave crossing time (evaluated for a CO WD in (Fuller & Lai 2013)) measures the magnetic coupling time and t_{gw} measures the gravitational wave inspiral timescale. Before solid body rotation is attained, another relevant timescale is the synchronization timescale t_s . For a tidal torque τ and tidal forcing frequency $\sigma = m(*)\Omega - \Omega_{spin}$, we note that angular momentum transfer is $\frac{\partial M_{sync}}{\partial t} \sigma R^2 = \tau$, where M_{sync} denotes the mass of the WD that has synchronized. Thus, the synchronization timescale is

$$t_{sync} \sim \frac{M_{sync} \sigma R^2}{\tau}, \\ \sim 2 \times 10^5 \text{ yr} \left(\frac{M}{M_\odot} \right) \left(\frac{\sigma}{2\pi/(1 \text{ hr})} \right) \left(\frac{R}{R_\oplus} \right)^2 \left(\frac{10^{-14} GM_\odot^2/R_\oplus}{\tau} \right). \quad (35)$$

A representative τ has been taken from (Burkart et al. 2013). However, since only the outer $\sim 10^{-4} M_\odot$ need be heated for the thermodynamically interesting effects studied in (Fuller & Lai 2013) and (Fuller & Lai 2012b), it seems that magnetic winding cannot absolutely rule out energetic outbursts such as tidal novae resulting from strong shear flows.

6.2 Applicability to Other Astrophysical Systems

[TODO flesh out]

- k_x, k_z : In astrophysical systems, $k_\perp \ll k_r$. While we do not explore different k_x, k_z, ω_1 in this study, with outgoing boundary conditions, there appears at first to be no z length scale other than k_z , so our results would seem to be invariant under rescaling of the z length scale. However, true turbulence is expected to be isotropic at small scales, which may couple k_x, k_z in a way that $k_x \ll k_z$ produces different dynamics than $k_x \lesssim k_z$ as we’ve studied. This is a numerically difficult regime though, so we defer consideration to future work.

- Validity of plane-parallel approximation? We’re all at $\geq 0.9 R_{WD}$.

- Solar-type stars (inner convective, outer radiative): different equation of state/stratification but could be qualitatively similar.

- Solar-type stars: In Barker & Ogilvie (2010), inwards-propagating IGW are excited that break via geometric focusing and effect synchronization. They find no reflected wave despite their nonlinear timescales being $10\times$ shorter than their viscous timescale.

It is not immediately clear whether our results here apply when the flux is geometrically focused, but as a hypothesis we assume the convergence in Figure 9 applies under geometric focusing as a zeroth approximation, perhaps as a property of the fluid motion within the geometrically thin critical layer.

Associating $t \sim \nu k^2 \approx \nu k_z^2$ with the viscous timescale and $t_{NL} \sim \mathbf{u} \cdot \nabla \sim \omega$ for the nonlinear timescale, we find their $\lambda = \frac{t_{NL}}{t_L} \sim Re$ our Reynolds number. Our simulations indicate $Re \gtrsim 500$ are required to observe the correct asymptotic behavior in terms of horizontal momentum flux reflection/transmission, so it is possible their lack of reflection is viscosity limited.

6.3 Heating

[TODO elaborate? Need to make plots to check?]

Our equations do not conserve energy, but it seems like more energy can be transmitted in higher modes as viscosity is decreased. Nevertheless, a significant fraction should still be dissipated in the critical layer since a significant energy cascade must happen in the critical layer.

7 ACKNOWLEDGEMENTS

REFERENCES

- Andrews D., McIntyre M. E., 1976, *Journal of the Atmospheric Sciences*, 33, 2031
- Ascher U. M., Ruuth S. J., Spiteri R. J., 1997, *Applied Numerical Mathematics*, 25, 151
- Barker A. J., Ogilvie G. I., 2010, *MNRAS*, 404, 1849
- Booker J. R., Bretherton F. P., 1967, *J. Fluid Mech.*, 27, 513–539
- Boyd J. P., 2001, *Chebyshev and Fourier spectral methods*. Courier Corporation
- Brown S., Stewartson K., 1982, *Journal of Fluid Mechanics*, 115, 217
- Burkart J., Quataert E., Arras P., Weinberg N. N., 2013, *Monthly Notices of the Royal Astronomical Society*, 433, 332
- Burns K. J., Vasil G. M., Oishi J. S., Lecoanet D., Brown B., 2016, *Dedalus: Flexible framework for spectrally solving differential equations*, *Astrophysics Source Code Library* (ascl:1603.015)
- Dosser H. V., Sutherland B. R., 2011a, *J. Atmos. Chem.*, 68, 2844
- Dosser H., Sutherland B., 2011b, *Physica D: Nonlinear Phenomena*, 240, 346
- Drazin P., 1977, *Proc. R. Soc. Lond. A*, 356, 411
- Fuller J., Lai D., 2011, *MNRAS*, 412, 1331
- Fuller J., Lai D., 2012a, *MNRAS*, 421, 426
- Fuller J., Lai D., 2012b, *ApJL*, 756, L17
- Fuller J., Lai D., 2013, *MNRAS*, 430, 274
- García-Berro E., Badenes C., Aznar-Siguán G., Lorén-Aguilar P., 2017, *MNRAS*, 468, 4815
- Gilfanov M., Bogdán Á., 2010, *Nature*, 463, 924
- Goldreich P., Nicholson P. D., 1989, *ApJ*, 342, 1079
- Hazel P., 1967, *J. Fluid Mech.*, 30, 775–783
- Iben Jr I., Tutukov A. V., 1984, *ApJS*, 54, 335
- Kilic M., Hambly N. C., Bergeron P., Genest-Beaulieu C., Rowell N., 2018, *MNRAS*, 479, L113
- Klostermeyer J., 1991, *Geophysical & Astrophysical Fluid Dynamics*, 61, 1
- Korol V., Rossi E. M., Groot P. J., Nelemans G., Toonen S., Brown A. G. A., 2017, *MNRAS*, 470, 1894
- Lecoanet D., Brown B. P., Zweibel E. G., Burns K. J., Oishi J. S., Vasil G. M., 2014, *The Astrophysical Journal*, 797, 94
- Lecoanet D., Vasil G. M., Fuller J., Cantiello M., Burns K. J., 2016, *Monthly Notices of the Royal Astronomical Society*, 466, 2181
- Lindzen R. S., Holton J. R., 1968, *Journal of the Atmospheric Sciences*, 25, 1095
- Maoz D., Sharon K., Gal-Yam A., 2010, *ApJ*, 722, 1879
- Nelemans G., 2009, *Class. Quantum Grav.*, 26, 094030
- Perets H. B., et al., 2010, *Nature*, 465, 322
- Shen K. J., et al., 2018, *AJ*, 865, 15
- Webbink R., 1984, *ApJ*, 277, 355
- Winters K. B., D’Asaro E. A., 1994, *J. Fluid Mech.*, 272, 255–284
- Wu Y., 1998, PhD thesis, California Institute of Technology
- Zahn J.-P., 1975, *A&A*, 41, 329

APPENDIX A: EQUATION IMPLEMENTATIONS

We denote $x \in [0, L_x]$, $z \in [0, L_z]$ the simulation domain and N_x, N_z the number of spectral modes in the respective dimensions.

Numerically, the nonlinear $\frac{\nabla P}{\rho}$ term is problematic: we desire a system where the fluid fields are not divided by one another. We introduce $\varpi = \frac{P}{\rho}$ instead, then mandate $\bar{\rho}, \bar{\varpi}_0$ background fields satisfy hydrostatic equilibrium $\nabla \varpi_0 + \varpi_0 \nabla \bar{\rho} + g\mathbf{z} = 0$. Taking isothermal stratification, we find $\varpi_0 = gH$. We further change variables to $\Upsilon = \ln \rho - \ln \bar{\rho}$ and $\varpi_1 = \varpi - \varpi_0$ deviations from the background state to obtain a system of equations at most quadratic in fluid fields:

$$\nabla \cdot \mathbf{u}_1 = 0, \quad (\text{A1a})$$

$$\frac{\partial \Upsilon}{\partial t} + (\mathbf{u}_1 \cdot \nabla) \Upsilon - \frac{u_z}{H} = 0, \quad (\text{A1b})$$

$$\frac{\partial u_x}{\partial t} + (\mathbf{u}_1 \cdot \nabla) u_x + \frac{\partial \varpi_1}{\partial x} + gH \frac{\partial \Upsilon}{\partial x} + \varpi_1 \frac{\partial \Upsilon}{\partial x} = 0, \quad (\text{A1c})$$

$$\frac{\partial u_z}{\partial t} + (\mathbf{u}_1 \cdot \nabla) u_z + \frac{\partial \varpi_1}{\partial z} + gH \frac{\partial \Upsilon}{\partial z} + \varpi_1 \frac{\partial \Upsilon}{\partial z} - \frac{\varpi_1}{H} = 0. \quad (\text{A1d})$$

It bears noting that these equations are exactly equivalent to the original Euler equations and hence conserve horizontal momentum.

A1 Artificial Dissipation

The nonlinear terms in the above equations will transfer energy from lower wavenumbers to higher wavenumbers. Since spectral codes have no numerical dissipation, artificial dissipation must be added. To ensure the dissipative system conserves horizontal momentum, we begin by adding dissipative terms to the flux-conservative form of the Euler fluid equations [Equation 1](#) (we use stress tensor $\tau_{ij} = P\delta_{ij}$):

$$\nabla \cdot \mathbf{u} = 0, \quad (\text{A2a})$$

$$\partial_t \rho + \nabla \cdot (\rho \mathbf{u} - \nu \nabla (\rho - \bar{\rho})) = 0, \quad (\text{A2b})$$

$$\partial_t (\rho \mathbf{u}) + \nabla \cdot (\rho \mathbf{u} \mathbf{u} + \text{diag}(\rho \varpi) - \nu \rho \nabla \mathbf{u}) + \rho g \mathbf{z} = 0. \quad (\text{A2c})$$

The same ν is used for both the diffusive and viscous term, though this is not required. Since the dissipation is not physical and is purely used for numerical stability, we choose it such that hydrostatic equilibrium is not modified. Some algebraic manipulation to re-cast it in the form of [Equation A1](#) gives

$$\nabla \cdot \mathbf{u} = 0, \quad (\text{A3a})$$

$$\partial_t \Upsilon + (\mathbf{u} \cdot \nabla) \Upsilon - \frac{u_z}{H} - \nu \left(\nabla^2 \Upsilon + (\nabla \Upsilon) \cdot (\nabla \Upsilon) - \frac{2}{H} \partial_z \Upsilon + \frac{1 - e^{-\Upsilon}}{H^2} \right) = 0, \quad (\text{A3b})$$

$$\begin{aligned} \partial_t \mathbf{u} + (\mathbf{u} \cdot \nabla) \mathbf{u} + \nabla \varpi + \varpi \nabla \Upsilon - \nu \nabla^2 \mathbf{u} + \mathbf{u} \nu \left(\nabla^2 \Upsilon + (\nabla \Upsilon) \cdot (\nabla \Upsilon) - \frac{2}{H} \partial_z \Upsilon + \frac{1 - e^{-\Upsilon}}{H^2} \right) \\ - 2\nu \left(((\nabla \Upsilon) \cdot \nabla) \mathbf{u} - \frac{1}{H} \partial_z \mathbf{u} \right) - \frac{\varpi_1}{H} = 0. \end{aligned} \quad (\text{A3c})$$

Hydrostatic equilibrium is still $\nabla \varpi_0 + g\mathbf{z} = 0$ where $\rho = \bar{\rho}, \mathbf{u} = 0$. Including the damping layers and forcing terms as described in [subsection 4.1](#), we finally obtain the full system of equations as simulated in Dedalus: [TODO update w/ mask]

$$\nabla \cdot \mathbf{u} = 0, \quad (\text{A4a})$$

$$\begin{aligned} \partial_t \Upsilon - \frac{u_z}{H} = \nu \left(\nabla^2 \Upsilon + (\nabla \Upsilon) \cdot (\nabla \Upsilon) - \frac{2}{H} \partial_z \Upsilon + \frac{1 - e^{-\Upsilon}}{H^2} \right), \\ - (\mathbf{u} \cdot \nabla) \Upsilon - \Gamma(z) \Upsilon + \frac{F}{\bar{\rho}(z)} e^{-\frac{(z-z_0)^2}{2\sigma^2}} \cos(k_x x - \omega t), \end{aligned} \quad (\text{A4b})$$

$$\begin{aligned} \frac{\partial u_x}{\partial t} + \frac{\partial T}{\partial x} + gH \frac{\partial \Upsilon}{\partial x} = \nu \nabla^2 u_x - u_x \nu \left(\nabla^2 \Upsilon + (\nabla \Upsilon) \cdot (\nabla \Upsilon) - \frac{2}{H} \partial_z \Upsilon + \frac{1 - e^{-\Upsilon}}{H^2} \right) \\ + 2\nu \left(((\nabla \Upsilon) \cdot \nabla) u_x - \frac{1}{H} \partial_z u_x \right) - \Gamma(z) u_x - (\mathbf{u} \cdot \nabla) u_x - T_1 \frac{\partial \Upsilon}{\partial x}, \end{aligned} \quad (\text{A4c})$$

$$\begin{aligned} \frac{\partial u_z}{\partial t} + \frac{\partial T}{\partial z} + gH \frac{\partial \Upsilon}{\partial z} - \frac{T_1}{H} = \nu \nabla^2 u_z - u_z \nu \left(\nabla^2 \Upsilon + (\nabla \Upsilon) \cdot (\nabla \Upsilon) - \frac{2}{H} \partial_z \Upsilon + \frac{1 - e^{-\Upsilon}}{H^2} \right) \\ + 2\nu \left(((\nabla \Upsilon) \cdot \nabla) u_z - \frac{1}{H} \partial_z u_z \right) - \Gamma(z) u_z - (\mathbf{u} \cdot \nabla) u_z - T_1 \frac{\partial \Upsilon}{\partial z}. \end{aligned} \quad (\text{A4d})$$